PHYSICAL REVIEW B **90**, 174111 (2014)

Piezoelectric enhancement of $(\mathrm{PbTiO_3})_m/(\mathrm{BaTiO_3})_n$ ferroelectric superlattices through domain engineering

Liang Hong,[1,*] Pingping Wu,[1,2] Yulan Li,[3] Venkatraman Gopalan,[1] Chang-Beom Eom,[4]
Darrell G. Schlom,[5] and Long-Qing Chen[1]
[1]*Department of Materials Science and Engineering, The Pennsylvania State University, University Park, Pennsylvania 16802, USA*
[2]*Department of Physics, University of Science and Technology Beijing, Beijing 100083, China*
[3]*Pacific Northwest National Laboratory, Richland, Washington 99352, USA*
[4]*Department of Materials Science and Engineering, University of Wisconsin-Madison, Madison, Wisconsin 53706, USA*
[5]*Department of Materials Science and Engineering and Kavli Institute at Cornell for Nanoscale Science,*
Cornell University, Ithaca, New York 14853, USA

(Received 22 October 2014; published 20 November 2014)

The phase diagram of $(\mathrm{PbTiO_3})_m/(\mathrm{BaTiO_3})_n$ ferroelectric superlattices was computed using the phase-field approach as a function of layer volume fraction and biaxial strain to tune ferroelectric properties through domain engineering. Two interesting domain structures are found: one with mixed Bloch-Néel-Ising domain wall structures and the other with stabilized monoclinic $\mathrm{M_c}$ phases. The polarization of the monoclinic $\mathrm{M_c}$ phase is able to rotate from out-of-plane to in-plane or vice versa under an electric field, and thus facilitates the domain reversal of rhombohedral domains. This contributes significantly to both reduced coercive fields and enhanced piezoelectric responses.

DOI: 10.1103/PhysRevB.90.174111 PACS number(s): 77.80.B−, 77.80.Dj, 77.65.−j

I. INTRODUCTION

Domain engineering is an effective approach to improving the functional properties of ferroelectric and piezoelectric materials [1–3]. One well-known example is the generation of large piezoelectric responses in the vicinity of the morphotropic phase boundary (MPB) in ferroelectric solid solutions, i.e., $\mathrm{Pb(Mg_{1/3}Nb_{2/3})O_3}$-$\mathrm{PbTiO_3}$ (PMN-PT) [2] and $\mathrm{PbZrO_3}$-$\mathrm{PbTiO_3}$ (PZT) [3], through an easy polarization rotation via an intermediate monoclinic phase [4–6]. Another example is the dramatically enhanced transition temperatures and enhanced ferroelectric properties made possible by engineering the domains and domain walls of ferroelectric thin films, using biaxial strains imposed by a substrate [7–9].

Superlattices, composed of two or more periodically repeated atomic/nanoscale oxide layers, offer additional degrees of freedom in addition to composition and strain, to engineer the domain structures and thus their responses under an external field. Indeed, enhanced permittivity [10] and recovery of ferroelectricity [11], originating from the complex phase interactions at the layer interfaces, have been discovered in superlattices [12,13]. Recently, polarization rotations were engineered by modulating the biaxial strain [14] and layer volume fraction [15] in $\mathrm{PbTiO_3/SrTiO_3}$ and $\mathrm{PbTiO_3/CaTiO_3}$ superlattices, respectively. The main objective of the present work is to determine whether enhanced piezoelectric responses, which are closely tied to dielectric permittivity, can be achieved through engineering the monoclinic phase by taking advantage of the electrostatic and elastic forces in ferroelectric superlattices.

To take into account the heterogeneity and domain formation in a superlattice, we calculate the phase diagram of $(\mathrm{PbTiO_3})_m/(\mathrm{BaTiO_3})_n$ $[(\mathrm{PTO})_m/(\mathrm{BTO})_n]$ ferroelectric superlattices using the phase-field approach [16]. Here, m and n denote the thickness, in unit cells, of the (001)-oriented $\mathrm{PbTiO_3}$ and $\mathrm{BaTiO_3}$ layers, respectively. Since there is a large difference between the pseudocubic lattice parameters of the two individual layers, there are many available substrates which can simultaneously exert tensile and compressive strains onto PTO and BTO layers, respectively. We aim to utilize this mixed strain states, tensile on one layer and compressive on the other, to produce in-plane and out-of-plane polarizations on each side of the interfaces between layers in a superlattice. The ferroelectric and piezoelectric responses of such a superlattice are obtained by applying an external electric field in a phase-field simulation. The focus of this paper is on the role of possible monoclinic domain states in enhancing the piezoelectric response and significantly decreasing the coercive fields of a superlattice.

II. MODEL

The periodically repeating unit of PTO and BTO layers in the superlattice is illustrated in Fig. 1. Each unit cell of a superlattice consists of m PTO and n BTO single-crystal unit cells along the thickness direction. We assume that the interfaces between PTO and BTO layers are coherent, and the superlattices are grown epitaxially on a substrate.

The total free energy, F, of a $(\mathrm{PTO})_m/(\mathrm{BTO})_n$ superlattice is expressed as

$$F = \int_V [f_{\mathrm{bulk}}(P_i) + f_{\mathrm{gra}}(P_{i,j}) + f_{\mathrm{elas}}(P_i,\varepsilon_{ij}) + f_{\mathrm{elec}}(P_i,E_i)]dV, \qquad (1)$$

where V is the representative volume, $P_i (i = 1,2,3)$ is the spontaneous polarization distribution, and f_{bulk} is the bulk free energy density of a ferroelectric using the paraelectric state as the reference state and expressed using an eighth-order

---

[*] lxh42@psu.edu

Landau-Devonshire polynomial in P_i,

$$\begin{aligned} f_{\text{bulk}}(P_i) = {} & \alpha_1(T)\left(P_1^2+P_2^2+P_3^2\right)+\alpha_{11}\left(P_1^4+P_2^4+P_3^4\right)+\alpha_{12}\left(P_1^2P_2^2+P_1^2P_3^2+P_2^2P_3^2\right)\\ & +\alpha_{111}\left(P_1^6+P_2^6+P_3^6\right)+\alpha_{112}\left[P_1^2\left(P_2^4+P_3^4\right)+P_2^2\left(P_1^4+P_3^4\right)+P_3^2\left(P_1^4+P_2^4\right)\right]\\ & +\alpha_{123}P_1^2P_2^2P_3^2+\alpha_{1111}\left(P_1^8+P_2^8+P_3^8\right)+\alpha_{1112}\left[P_1^6\left(P_2^2+P_3^2\right)+P_2^6\left(P_1^2+P_3^2\right)+P_3^6\left(P_1^2+P_2^2\right)\right]\\ & +\alpha_{1122}\left(P_1^4P_2^4+P_2^4P_3^4+P_1^4P_3^4\right)+\alpha_{1123}\left(P_1^4P_2^2P_3^2+P_2^4P_3^2P_1^2+P_3^4P_1^2P_2^2\right), \end{aligned} \tag{2}$$

in which only α_1 is assumed to be temperature dependent, and all the coefficients are obtained from the stress-free condition.

The gradient energy density f_{gra} in Eq. (1) is

$$f_{\text{gra}}(P_{i,j}) = \tfrac{1}{2}G_{ijkl}P_{i,j}P_{k,l}, \tag{3}$$

where $P_{i,j} = \partial P_i/\partial x_j$ and G_{ijkl} is the gradient energy coefficient. In this paper, the Einstein implied summation convention is employed.

The elastic energy density f_{elas} is

$$f_{\text{elas}}(P_i,\varepsilon_{ij}) = \tfrac{1}{2}c_{ijkl}\left(\varepsilon_{ij}-\varepsilon_{ij}^0\right)\left(\varepsilon_{kl}-\varepsilon_{kl}^0\right), \tag{4}$$

where c_{ijkl} is the elastic stiffness tensor. The eigenstrain is composed by two parts [17,18], i.e., $\varepsilon_{ij}^0 = Q_{ijkl}P_kP_l + \varepsilon_{ij}^{\text{latt}}$, where Q_{ijkl} is the electrostrictive coefficient and $\varepsilon_{ij}^{\text{latt}} = (a(\vec{r}) - a_{\text{ref}})/a_{\text{ref}}$ represents the lattice mismatch between the two layers (BTO is taken as the reference layer, $a_{\text{ref}} = a_{\text{BTO}}$). The total strain is $\varepsilon_{ij} = \bar{\varepsilon}_{ij} + \eta_{ij}$, where $\bar{\varepsilon}_{ij}$ is the homogeneous strain, and η_{ij} is the heterogeneous strain. The biaxial strains are imposed along the x_1 and x_2 directions, i.e., $\bar{\varepsilon}_{11} = \bar{\varepsilon}_{22} = (a_{\text{sub}} - a_{\text{ref}})/a_{\text{ref}}$ and $\bar{\varepsilon}_{12} = 0$. The other homogeneous strains are calculated to satisfy $[\int_V c_{i3kl}(\varepsilon_{kl} - \varepsilon_{kl}^0)dV]/V = 0$, i.e., the average stress components are zero. The microelasticity theory [19] of Khachaturyan and Shatalov together with an iterative method [20] is utilized to get the elastic solution through the mechanical equilibrium condition $\sigma_{ij,j} = 0$.

The expression for f_{elec} is given by

$$f_{\text{elec}}(P_i,E_i) = -\left(\tfrac{1}{2}\varepsilon_0 k_b E_i^2 + E_iP_i\right), \tag{5}$$

in which ε_0 is the vacuum permittivity. The dielectric constant of the vacuum is adopted, i.e., $k_b = 1$, in the present study. There is no obvious difference between the results obtained with $k_b = 1$ and $k_b = 10$. The total electric field E_i is composed of electrostatic field E_i^{sta} generated from the internal bound charges and external electric field E_i^{ext}. The top surface and the superlattice/substrate interface are assumed to be perfectly charge compensated. The electrostatic equilibrium equation $\varepsilon_0 k_b \varphi_{,ii} = P_{i,i}$ is solved to obtain the electrostatic potential through $E_i = -\varphi_{,i}$.

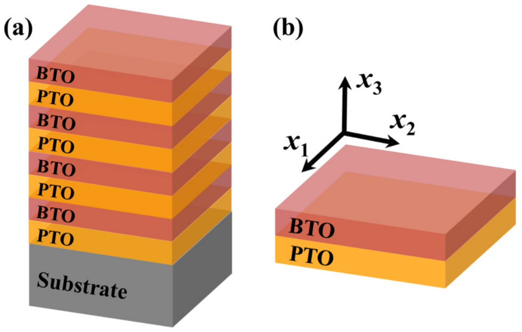

FIG. 1. (Color online) Schematic of (a) a $(\text{PTO})_m/(\text{BTO})_n$ ferroelectric superlattice on a substrate and (b) the simulation cell.

The spatial variation of the spontaneous polarizations in the superlattice is determined by the time-dependent Ginzburg-Landau (TDGL) equation,

$$\frac{\partial P_i(x,t)}{\partial t} = -L\frac{\delta F}{\delta P_i(x,t)}, \tag{6}$$

where L is the kinetic coefficient.

The simulation box of a $(\text{PTO})_m/(\text{BTO})_n$ superlattice unit cell is discretized as $64\Delta x_1 \times 64\Delta x_2 \times N\Delta x_3$, where $\Delta x_1 = \Delta x_2 = 1\text{nm}$, $\Delta x_3 = 0.5a_{\text{BTO}} \approx 0.2\text{nm}$ and $N = 2(m+n)$. The gradient energy coefficients are assumed to be isotropic with the nonzero ones $G_{11}/G_0 = 2.0$, $G_{44}/G_0 = 1.0$. G_{ij} is the Voigt notation for G_{ijkl}.G_0 is related to Δx_1 by $\Delta x_1 = \sqrt{G_0/|\alpha_1^{\text{BTO}}|_{T=27^\circ\text{C}}}$. The other physical parameters are summarized in Ref. [21] obtained from Refs. [22–26]. Periodic boundary conditions are employed along x_1, x_2, and x_3 directions. The semi-implicit Fourier-spectral method [27] is used to solve the TDGL equation. All the simulations start from an initial paraelectric state with random noise perturbations for the local polarization.

III. RESULTS AND DISCUSSION

The four representative domain structures of $(\text{PTO})_m/(\text{BTO})_n$ superlattices obtained from the phase-field simulations are shown in Fig. 2 under different substrate constraints $e_0 = \bar{\varepsilon}_{11} = \bar{\varepsilon}_{22}$. These domain structures correspond to near equilibrium states, i.e., no significant changes take place with prolonged annealing. The letters T, R, M, and O indicate tetragonal, rhombohedral, monoclinic, and orthorhombic crystallographic symmetries, respectively. The subscript "op" or "ip" of T indicates whether a tetragonal phase has out-of-plane or in-plane polarizations, respectively. A type A domain structure is composed of T_{op} domains with Ising-type domain walls, i.e., the polarization directions are in opposite directions on each side of the domain wall with the magnitude of polarization gradually changing across the domain wall. A type B domain structure consists of a mixture of $\text{T}_{\text{op}} + \text{R}$ domains, in which mixed Bloch-Néel-Ising domain walls [13] connect the T and R domains across their interfaces in the superlattice. Such a mixed type of domain wall exhibits 180° polarization rotation with polarization components both in a plane parallel (Bloch-type) and normal (Néel-type) to the plane of domain wall, in addition to the Ising-type P_3 components. A type C domain structure is mainly composed of an M_c phase with $(P_1,0,P_3)$ or $(0,P_2,P_3)$ polarizations. Type D is a mixture of $\text{T}_{\text{ip}} + \text{O}$ domains in

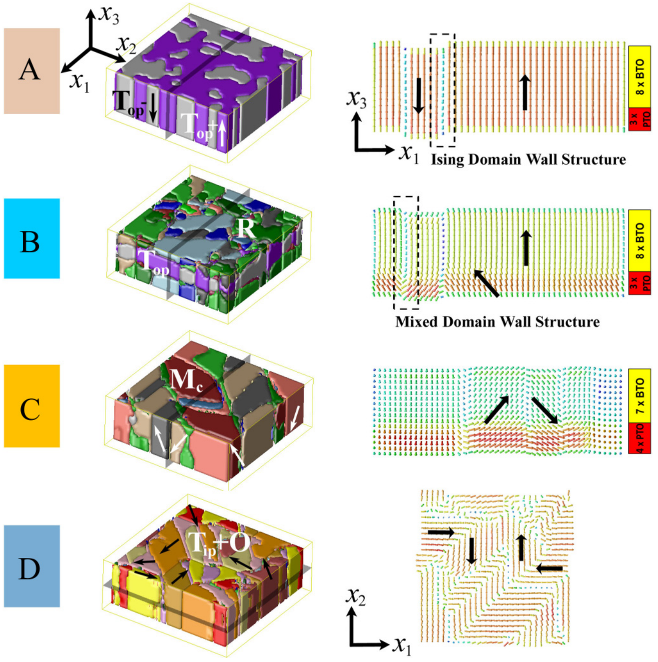

FIG. 2. (Color online) Representative domain structures of $(PTO)_m/(BTO)_n$ superlattices under different substrate constrains (e_0) at ambient conditions. Domain definitions and the corresponding polarizations: $T_{op}(0,0,P_3)$, $T_{ip}(P_1,0,0)/(0,P_2,0)$, $R(P_1,P_1,P_3)$, $M_c(P_1,0,P_3)/(0,P_2,P_3)$, and $O(P_1,P_2,0)$. The domain structures of A, B, C, and D correspond to T_{op} in a $(PTO)_3/(BTO)_8$ superlattice on a (001) $SrTiO_3$ substrate with $e_0 = -0.023$, $T_{op} + R$ in a $(PTO)_3/(BTO)_8$ superlattice on a (110) $DyScO_3$ substrate with $e_0 = -0.012$, M_c in a $(PTO)_4/(BTO)_7$ superlattice on a (110) $GdScO_3$ substrate with $e_0 = -0.007$, and $T_{ip} + O$ in a $(PTO)_4/(BTO)_7$ superlattice on a substrate ($a_{sub} = 4.01$ Å) with $e_0 = 0.004$, respectively. The polarization vector maps in the indicated cross-sectional planes are shown at the right.

which only in-plane polarizations exist. The two-dimensional polarization vector maps are included to show the polarization rotation and different domain wall structures.

The phase diagram of $(PTO)_m/(BTO)_n$ ($m + n = 11$) superlattices as a function of substrate lattice parameter (a_{sub}) for an m-unit-cell-thick PTO layer is presented in Fig. 3. The lattice parameters for a number of commonly used substrates are indicated in the diagram [28]. The epitaxial strains imparted by the substrate on the individual layers range from -0.011 to 0.019 for the PTO layer and -0.026 to 0.004 for the BTO layer based on the range of a_{sub} shown in Fig. 3. For large compressive strains, the stripe T_{op} domains (pattern A) are stable. The out-of-plane polarization is almost uniform across the superlattice due to the electrostatic coupling between the two layers. On the other hand, under large tensile strains T_{ip} and O domains (pattern D) become stable, consistent with the phase diagrams of PTO and BTO thin films [25,29]. Interestingly, two intermediate domain patterns (B and C) exist. These two types of domain states result from the combined effects of elastic and electrostatic couplings in the superlattice. The polarizations in the two layers prefer to be orthogonal due to the opposite (tensile and compressive) states of the individual PTO and BTO layers, whereas the minimization of the depolarization field requires continuity of the out-of-plane polarization. The stability of these intermediate domain structures requires the two layers to possess large spontaneous polarizations and to have a large difference between their pseudocubic lattice parameters. For example, no monoclinic phase was observed in $PbTiO_3/SrTiO_3$ superlattices [14], since the tensile $SrTiO_3$ layers give O domains with weak polarizations. On the contrary, the tensile strains in PTO layers of $(PTO)_m/(BTO)_n$ superlattices prefer T_{ip} and the in-plane polarizations are strong.

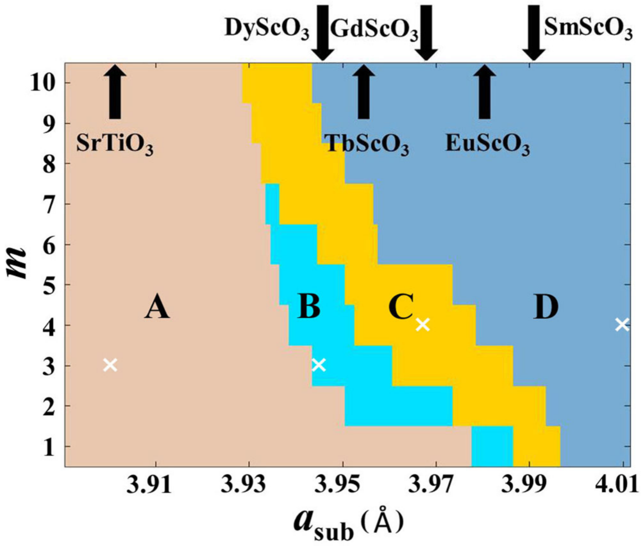

FIG. 3. (Color online) Strain phase diagram of $(PTO)_m/(BTO)_n$ superlattices with $m + n = 11$ as a function of the pseudocubic lattice parameter of the substrate (a_{sub}) and an m-unit-cell-thick PTO layer at room temperature. The × indicates the locations of the domain structures shown in Fig. 2. The symbols A, B, C, and D represent the phases of the superlattices possessing the four representative domain structures.

Another approach to engineering domain structures in superlattices is tuning the volume fraction of each individual layer. The stability of the four types of domain structures evolves from A→B→C→D as the PTO layer thickness increases and a_{sub} lies between 3.94 Å$\leqslant a_{sub} \leqslant$3.97 Å (Fig. 3). Within this range of substrate lattice parameters, PTO layers are under tensile strain, and the BTO layers are under compressive strain. As the PTO layer increases in thickness, the in-plane polarizations firstly nucleate at the interfaces [13,30] between layers and then grow into a mixture of $T_{op} + R$ (pattern B). Since the out-of-plane polarization of the BTO layers is large, the enhanced in-plane polarization of superlattices with thicker PTO layers leads to a stabilization of the monoclinic M_c domain structures (pattern C).

The stability of domain structures in the superlattices is sensitive to the strain states in the PTO layers. For example, the intermediate M_c phases are found to bridge the T_{op} and R domain states in $PbTiO_3/CaTiO_3$ superlattices grown on a $SrTiO_3$ substrates [15], in which the PTO layers are under compression. Pure PTO under pressure also shows a similar phase transition sequence [31]. On the other hand, the PTO layers in our $(PTO)_m/(BTO)_n$ superlattices are under tensile strain, and the M_c phases bridge the R and $T_{ip} + O$ domain states. The low-symmetry M_c phases are stabilized by the

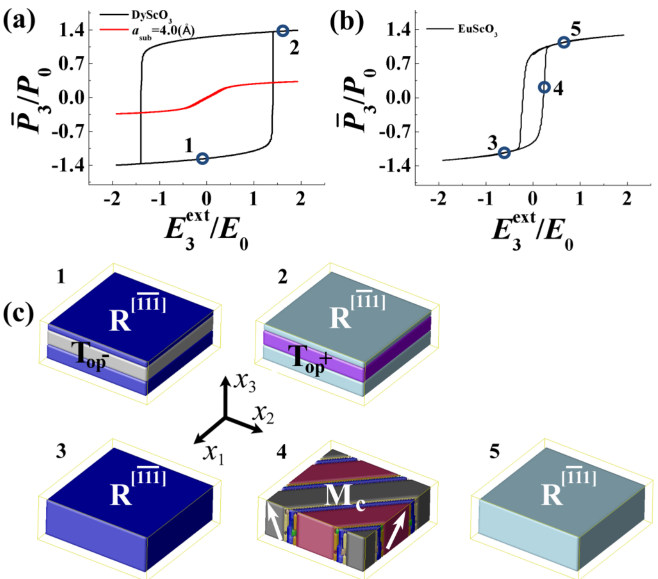

FIG. 4. (Color online) *P-E* hysteresis loops of a (PTO)$_3$/(BTO)$_8$ superlattice commensurately strained to (a) a (110) DyScO$_3$ substrate and to a substrate with an in-plane lattice parameter 4.0 Å and (b) a (110) EuScO$_3$ substrate. The corresponding domain structures at the positions of the five circles are shown in (c). The superscript of R denotes the polarization variant of rhombohedral phase.

cooperative effect of elastic and electrostatic fields. Similarly, in a thin PTO film, which is under tensile strain, the T$_{ip}$ phase rotates to become the M$_c$ phase due to the residual depolarization field [32].

To explore the piezoelectric response of superlattices, we calculate the variations of the average polarization ($\bar{P}_3$) and strain ($\bar{\varepsilon}_{33}$) of superlattices in response to an external electric field (E^{ext}), i.e., polarization-electric field (*P-E*) and strain-electric field (ε-*E*) hysteresis loops as shown in Figs. 4 and 5. Figure 5(a) gives the schematic of the computational method. The piezoelectric response of a superlattice with a negative remnant polarization state is calculated, around which polarization rotation without obvious phase transition contributes the most to the piezoelectric response. We use $P_0 = 0.26\,\text{C/m}^2$, $E_0 = 50\,\text{MV/m}$, and $d_{33}^0 = 12.0\,\text{pm/V}$ to normalize the calculated values. Here, d_{33}^0 is the calculated piezoelectric response of a (PTO)$_3$/(BTO)$_8$ superlattice constrained to a (001) SrTiO$_3$ substrate.

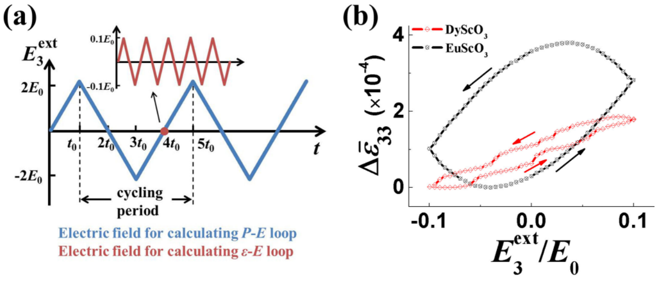

FIG. 5. (Color online) (a) A schematic depicting the computational method used to calculate *P-E* and ε-*E* loops. The *P-E* loop is obtained using a triangle-wave electric field along the thickness direction, whose amplitude and frequency are $2E_0$ and $1/4t_0$, respectively. Here, t_0 represents 40000 simulation steps. A modulated AC field of amplitude $0.1E_0$ and frequency $50t_0$ is superposed onto the field at the negative remnant polarization state to calculate the oscillatory deformation of the superlattices, resulting in the calculated ε-*E* loop. (b) The ε-*E* loops calculated for a (PTO)$_3$/(BTO)$_8$ superlattice commensurately strained to a (110) DyScO$_3$ substrate and to a (110) EuScO$_3$ substrate.

The regular *P-E* hysteresis loop shown in Fig. 4(a) is calculated for (PTO)$_m$/(BTO)$_n$ superlattices possessing mixed Bloch-Néel-Ising domain walls (pattern B in Fig. 3). This is different from the constricted hysteresis loop of BaTiO$_3$/SrTiO$_3$ superlattices constrained to a GdScO$_3$ substrate [33], in which the stripe domains with mixed domain walls are expected around zero E^{ext}. Figure 4(b) presents a slim calculated hysteresis loop, which is commonly observed in relaxor ferroelectrics [34,35], with a remarkably decreased coercive field (E_{coer}). This much smaller E_{coer} is attributed to the presence of a monoclinic M$_c$ phase in the vicinity of the E_{coer} during the 71° polarization reversal [see Fig. 4(c)], because the enhanced in-plane polarization components of the M$_c$ phase can lead to additional driving forces for the nucleation of reverse domains. This monoclinic M$_c$ phase is completely stabilized by competitive long-range elastic and electrostatic fields, rather than a local pinning interaction from structural inhomogeneity [36]. It also allows a significant improvement of the calculated effective piezoelectric response as discussed later. Compared to E_{coer}, the decrease in the value of the calculated remnant polarization (P_r) is much smaller, since only the reversal of the out-of-plane polarization is calculated to occur during the reversal, while the in-plane components remain largely unchanged. For superlattices with domain pattern A, regular hysteresis loops with large E_{coer} are calculated (not shown here). The calculated *P-E* loop of superlattices possessing domain pattern D [the red curve in Fig. 4(a)] shows nonlinear dielectric behavior.

To probe the expected influence of the domain structures on the piezoelectric response, we calculate the ε-*E* loops of the superlattices on various substrates. The calculated strain variation $\Delta\bar{\varepsilon}_{33}$ is shown in Fig. 5(b). For the (PTO)$_3$/(BTO)$_8$ superlattice commensurately strained to DyScO$_3$, the calculated strain varies with electric field quasi-linearly with significant hysteresis. The small slope in this linear loop suggests a difficult polarization rotation in the stable single domain under the external field. On the EuScO$_3$ substrate, the calculated ε-*E* loop has a rounded-rectangular form with steeper slopes, indicating an easier polarization rotation between R and M$_c$ (as shown in Fig. 4). The calculated piezoelectric coefficient ($d_{33} = \Delta\bar{\varepsilon}_{33}|_{\max}/0.2E_0$) is enhanced accordingly. The calculated ferroelectric and piezoelectric properties of (PTO)$_3$/(BTO)$_8$ superlattices as a function of the pseudocubic lattice parameter of the substrate are summarized in Fig. 6. The calculated values of both E_{coer} and P_r decreases monotonically with the increase in a_{sub}. This is consistent with the calculated trends in other ferroelectrics, in which applying a compressive strain expands the calculated *P-E* hysteresis loops and application of a tensile stain contracts them [37,38]. The maximum d_{33} together with a slim *P-E* loop are calculated to occur around the phase boundary between domain structures C and D, indicating a phase transition mediated by the M$_c$ phase. On the right side of the phase boundary, the calculated value of

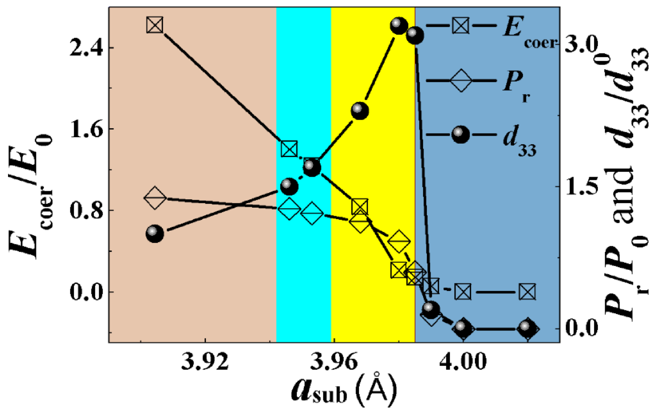

FIG. 6. (Color online) Variations of the calculated coercive field (E_{coer}), remnant polarization (P_r) and piezoelectric constant (d_{33}) of $(PTO)_3/(BTO)_8$ superlattices constrained to the pseudocubic lattice parameter of the substrate. The background colors differentiating the domain patterns correspond to the phase diagram in Fig. 3.

d_{33} significantly decreases due to the dielectric behavior shown in Fig. 4(a). Therefore it is important to engineer superlattices close to the phase boundary between domain structures C and D to enhance their piezoelectric responses.

IV. CONCLUSIONS

The phase diagram of $(PbTiO_3)_m/(BaTiO_3)_n$ ferroelectric superlattices as a function of layer volume fraction and the pseudocubic lattice parameter of the substrate is calculated using the phase-field approach. The two ferroelectric layers are strongly coupled by the elastic and electrostatic fields, and two interesting domain structures, i.e., one with mixed Bloch-Néel-Ising domain walls and the other with stable monoclinic M_c phases, are found. The calculated hysteresis loops show that M_c domains bridge the 71° domain reversal of the rhombohedral phases, contributing significantly to decreased $E_{coer}$and enhanced d_{33}, while maintaining similar P_r. The present study provides a novel approach to enhancing piezoelectric responses through engineering monoclinic M_c phases in ferroelectric superlattices.

ACKNOWLEDGMENTS

L. Hong would like to thank F. Xue, J. Britson, and J. M. Hu for useful discussions. L. Hong would also like to thank the support from a DOE Computational Materials and Chemical Sciences Network Grant through Argonne National Lab. This work was supported by the National Science Foundation (NSF) under Grants DMR-0820404, DMR-1210588, and DMR-1234096. The computer simulations were carried out on the LION and cyberstar clusters at the Pennsylvania State University, in part supported by instrumentation (cyberstar Linux cluster) funded by the NSF through Grant OCI-0821527.

---

[1] X. B. Ren, Nat. Mater. **3**, 91 (2004).

[2] S. E. Park and T. R. Shrout, J. Appl. Phys. **82**, 1804 (1997).

[3] B. Jaffe, R. S. Roth, and S. Marzullo, J. Appl. Phys. **25**, 809 (1954).

[4] H. Fu and R. E. Cohen, Nature (London) **403**, 281 (2000).

[5] B. Noheda, D. E. Cox, G. Shirane, J. Gao, and Z. G. Ye, Phys. Rev. B **66**, 054104 (2002).

[6] B. Noheda, D. E. Cox, G. Shirane, J. A. Gonzalo, L. E. Cross, and S. E. Park, Appl. Phys. Lett. **74**, 2059 (1999).

[7] J. Wang, J. B. Neaton, H. Zheng, V. Nagarajan, S. B. Ogale, B. Liu, D. Viehland, V. Vaithyanathan, D. G. Schlom, U. V. Waghmare, N. A. Spaldin, K. M. Rabe, M. Wuttig, and R. Ramesh, Science **299**, 1719 (2003).

[8] K. J. Choi, M. Biegalski, Y. L. Li, A. Sharan, J. Schubert, R. Uecker, P. Reiche, Y. B. Chen, X. Q. Pan, V. Gopalan, L. Q. Chen, D. G. Schlom, and C. B. Eom, Science **306**, 1005 (2004).

[9] J. H. Haeni, P. Irvin, W. Chang, R. Uecker, P. Reiche, Y. L. Li, S. Choudhury, W. Tian, M. E. Hawley, B. Craigo, A. K. Tagantsev, X. Q. Pan, S. K. Streiffer, L. Q. Chen, S. W. Kirchoefer, J. Levy, and D. G. Schlom, Nature (London) **430**, 758 (2004).

[10] H. N. Lee, H. M. Christen, M. F. Chisholm, C. M. Rouleau, and D. H. Lowndes, Nature (London) **433**, 395 (2005).

[11] M. Dawber, N. Stucki, C. Lichtensteiger, S. Gariglio, P. Ghosez, and J. M. Triscone, Adv. Mater. **19**, 4153 (2007).

[12] E. Bousquet, M. Dawber, N. Stucki, C. Lichtensteiger, P. Hermet, S. Gariglio, J. M. Triscone, and P. Ghosez, Nature (London) **452**, 732 (2008).

[13] D. Lee, R. K. Behera, P. Wu, H. Xu, Y. L. Li, S. B. Sinnott, S. R. Phillpot, L. Q. Chen, and V. Gopalan, Phys. Rev. B **80**, 060102 (2009).

[14] P. Aguado-Puente, P. García-Fernández, and J. Junquera, Phys. Rev. Lett. **107**, 217601 (2011).

[15] J. Sinsheimer, S. J. Callori, B. Bein, Y. Benkara, J. Daley, J. Coraor, D. Su, P. W. Stephens, and M. Dawber, Phys. Rev. Lett. **109**, 167601 (2012).

[16] L. Q. Chen, Annu. Rev. Mater. Res. **32**, 113 (2002).

[17] Y. L. Li, S. Y. Hu, D. Tenne, A. Soukiassian, D. G. Schlom, X. X. Xi, K. J. Choi, C. B. Eom, A. Saxena, T. Lookman, Q. X. Jia, and L. Q. Chen, Appl. Phys. Lett. **91**, 112914 (2007).

[18] F. Xue, J. J. Wang, G. Sheng, E. Huang, Y. Cao, H. H. Huang, P. Munroe, R. Mahjoub, Y. L. Li, V. Nagarajan, and L. Q. Chen, Acta Mater. **61**, 2909 (2013).

[19] A. G. Khachaturyan and G. A. Shatalov, Sov. Phys. JETP **29**, 557 (1969).

[20] S. Y. Hu and L. Q. Chen, Acta Mater. **49**, 1879 (2001).

[21] For PTO: $\alpha_1=3.8(T-479)\times 10^5$, $\alpha_{11}=-7.3\times 10^7$, $\alpha_{12}=7.5\times 10^8$, $\alpha_{111}=2.6\times 10^8$, $\alpha_{112}=6.1\times 10^8$, $\alpha_{123}=-3.7\times 10^9$, $\alpha_{1111}=\alpha_{1112}=\alpha_{1122}=\alpha_{1123}=0.0$, $c_{11}=1.746\times 10^{11}$, $c_{12}=0.794\times 10^{11}$, $c_{44}=1.111\times 10^{11}$, $Q_{11}=0.089$, $Q_{12}=-0.026$, $Q_{44}=0.0675$, $a=3.935\times 10^{-10}+7.312(T-25)\times 10^{-15}$; For BTO: $\alpha_1=4.124(T-115)\times 10^5$,

$\alpha_{11} = -2.097 \times 10^8$, $\alpha_{12} = 7.974 \times 10^8$, $\alpha_{111} = 1.294 \times 10^9$, $\alpha_{112} = -1.95 \times 10^9$, $\alpha_{123} = -2.5 \times 10^9$, $\alpha_{1111} = 3.863 \times 10^{10}$, $\alpha_{1112} = 2.529 \times 10^{10}$, $\alpha_{1122} = 1.637 \times 10^{10}$, $\alpha_{1123} = 1.367 \times 10^{10}$, $c_{11} = 1.78 \times 10^{11}$, $c_{12} = 0.964 \times 10^{11}$, $c_{44} = 1.22 \times 10^{11}$, $Q_{11} = 0.1$, $Q_{12} = -0.034$, $Q_{44} = 0.0295$, $a = 3.994 \times 10^{-10} + 5.35386T \times 10^{-15}$, where a is the pseudocubic lattice parameter, c_{ij} and Q_{ij} are the Voigt notation for c_{ijkl} and Q_{ijkl} (in SI units and T is in °C).

[22] M. J. Haun, E. Furman, S. J. Jang, H. A. McKinstry, and L. E. Cross, J. Appl. Phys. **62**, 3331 (1987).

[23] N. A. Pertsev, A. G. Zembilgotov, and A. K. Tagantsev, Phys. Rev. Lett. **80**, 1988 (1998).

[24] Y. L. Li, L. E. Cross, and L. Q. Chen, J. Appl. Phys. **98**, 064101 (2005).

[25] Y. L. Li and L. Q. Chen, Appl. Phys. Lett. **88**, 072905 (2006).

[26] P. E. Janolin, F. L. Marrec, J. Chevreu, and B. Dkhil, Appl. Phys. Lett. **90**, 192910 (2007).

[27] L. Q. Chen and J. Shen, Comput. Phys. Commun. **108**, 147 (1998).

[28] D. G. Schlom, L. Q. Chen, C. J. Fennie, V. Gopalan, D. A. Muller, X. Q. Pan, R. Ramesh, and R. Uecker, MRS Bull. **39**, 118 (2014).

[29] Y. L. Li, S. Y. Hu, Z. K. Liu, and L. Q. Chen, Appl. Phys. Lett. **78**, 3878 (2001).

[30] P. Zubko, N. Jecklin, A. Torres-Pardo, P. Aguado-Puente, A. Gloter, C. Lichtensteiger, J. Junquera, O. Stéphan, and J. M. Triscone, Nano Lett. **12**, 2846 (2012).

[31] M. Ahart, M. Somayazulu, R. E. Cohen, P. Ganesh, P. Dera, H. Mao, R. J. Hemley, Y. Ren, P. Liermann, and Z. Wu, Nature **451**, 545 (2008).

[32] G. Catalan, A. Janssens, G. Rispens, S. Csiszar, O. Seeck, G. Rijnders, D. H. A. Blank, and B. Noheda, Phys. Rev. Lett. **96**, 127602 (2006).

[33] P. Wu, X. Ma, Y. Li, V. Gopalan, and L. Q. Chen, Appl. Phys. Lett. **100**, 092905 (2012).

[34] L. E. Cross, Ferroelectrics **76**, 241 (1987).

[35] T. Kim, J. N. Hanson, A. Gruverman, A. I. Kingon, and S. K. Streiffer, Appl. Phys. Lett. **88**, 262907 (2006).

[36] Y. Gu, F. Xue, S. Lei, T. T. A. Lummen, J. Wang, V. Gopalan, and L. Q. Chen, Phys. Rev. B **90**, 024104 (2014).

[37] S. Choudhury, Y. L. Li, L. Q. Chen, and Q. X. Jia, Appl. Phys. Lett. **92**, 142907 (2008).

[38] S. P. Beckman, X. Wang, K. M. Rabe, and D. Vanderbilt, Phys. Rev. B **79**, 144124 (2009).